Quantum Anomalous Hall Effect with Tunable Chern Numbers in High-Temperature 1T-PrN_2 Monolayer

Xu-Cai Wu(吴绪才), Shu-Zong Li(李树宗), Jun-Shan Si(司君山), Bo Huang(黄博), and Wei-Bing Zhang(张卫兵)*

Hunan Provincial Key Laboratory of Flexible Electronic Materials Genome Engineering, School of Physics and Electronic Sciences, Changsha University of Science and Technology, Changsha 410114, China

(Received 17 February 2024; accepted manuscript online 28 April 2024)

Quantum anomalous Hall (QAH) insulators have highly potential applications in spintronic device. However, available candidates with tunable Chern numbers and high working temperature are quite rare. Here, we predict a 1T-PrN_2 monolayer as a stable QAH insulator with high magnetic transition temperature of above 600 K and tunable high Chern numbers of $C = \pm 3$ from first-principles calculations. Without spin-orbit coupling (SOC), the 1T-PrN_2 monolayer is predicted to be a p-state Dirac half metal with high Fermi velocity. Rich topological phases depending on magnetization directions can be found when the SOC is considered. The QAH effect with periodical changes of Chern number (± 1) can be produced when the magnetic moment breaks all twofold rotational symmetries in the xy plane. The critical state can be identified as Weyl half semimetals. When the magnetization direction is parallel to the z-axis, the system exhibits high Chern number QAH effect with $C = \pm 3$. Our work provides a new material for exploring novel QAH effect and developing high-performance topological devices.

DOI: 10.1088/0256-307X/41/5/057303

Quantum anomalous Hall (QAH) effect [1–4] has attracted extensive attention due to its peculiar dissipation-free chiral edge states. Experimentally, QAH was first observed in Cr-doped $(Bi,Sb)_2Te_3$. However, the working temperature is only 30 mK [5] since the reduced sample quality induced by doping. [6–8] Most recently, the intrinsic QAH effect was realized in $MnBi_2Te_4$ thin films, but it is still far away from practical applications due to the minimal band gap of 50 meV and the low observable temperature of 1.4 K. [9,10]

On the other hand, it is well known that QAH can be characterized by the Chern number. Its magnitude and sign correspond to the number and direction of the dissipation-free conducting channels on the edge. Realizing materials with high Chern numbers allow for fabrication of high performance QAH devices. Various strategies such as changing the atomic layer number, doping concentrations, and the stacking order [11–15] have been proposed for adjusting the Chern numbers. It should be noticed that the Chern number for a specified structure is generally fixed. Recently, magnetization direction dependent Chern number without altering the structures has attracted much attention. Some QAH materials, such as $NiAsO_3$, [16] YN_2, [17–19] and rare-earth metal dinitrides, [20,21] have been reported. However, candidates with tunable high Chern numbers are still scarce at present. Therefore, it is crucial to explore QAH materials with both tunable high Chern number and high magnetization transition temperatures.

In this Letter, we propose a 1T-phase PrN_2 monolayer as a stable QAH insulator with tunable Chern numbers and high magnetic transition temperature. When the magnetization lies in xy plane and breaks all the three twofold rotational symmetries, the QAH states with low Chern numbers ($C = \pm 1$) are generated. When the magnetization is parallel to z-axis, the band gap increases to 101.12 meV and enters the QAH phase with high Chern numbers ($C = \pm 3$). These rich topological properties are predicted in the 1T-phase PrN_2 monolayer that is taken as one of the candidate materials for potential applications in spintronics.

Computational Details. The present calculations have been performed using the Vienna *ab initio* simulation package code (VASP) [22,23] within the projector augmented-wave method. [24,25] General gradient approximations in the Perdew–Burke–Ernzerhof (PBE) implementation [26] are employed as the exchange-correlation functional. After convergence test shown in Figs. S1–S3 of the Supplementary Material, the plane-wave basis with a kinetic energy cutoff of 500 eV and Γ-centered Monkhorst–Pack grids of $21 \times 21 \times 1$ [27] were used in our calculation. The structure relaxation including both the atomic positions and lattice vectors is performed by the conjugate gradient scheme until the maximum force on each atom is less than 0.001 eV/Å and the total energy was converged to 1×10^{-8} eV with the Gaussian smearing method. The vacuum layer is set to 20 Å to avoid unnecessary interactions between the periodic layers. During calculations, we used the recommended pseudopotentials with the electronic configuration $2s^2 2p^3$ for N and $5s^2 5p^6 5d^1 6s^2$ for

*Corresponding author. Email: zhangwb@csust.edu.cn
© 2024 Chinese Physical Society and IOP Publishing Ltd

Pr. The phonon calculations have been performed using the finite displacement approach, as implemented in the Phonopy code,[28] in which a $3 \times 3 \times 1$ supercell and a displacement of 0.01 Å from the equilibrium atomic positions are employed. The *ab initio* molecular-dynamics (AIMD) simulations are performed with a $4 \times 4 \times 1$ supercell by using a Nosé heat bath scheme in a canonical ensemble at 300 K to examine the thermal stability of PrN_2 monolayer. The maximally localized Wannier functions (MLWFs) constructed by the WANNIER90[29] package are employed to obtain the Berry curvatures. The Chern numbers are calculated by the VASPBERRY code[30,31] and verified by WannierTools.[32] The edge states and the anomalous Hall conductivity (AHC) are calculated with WannierTools.

Structure and Stability. As shown in Figs. 1(a)–1(c), the 1T PrN_2 monolayer possesses a hexagonal structure with the space group of $P\bar{3}m1$ (No. 164, D^3_{3d}). Each Pr atom forms an octahedral structure with six surrounding N atoms as shown in Fig. 1(a). The optimized lattice constant is 3.98 Å. Compared to previous studies, it is smaller than 4.06 Å of LaN_2[33] and larger than those of NdN_2 (3.776 Å),[21] GdN_2 (3.74 Å),[34] TbN_2-LuN_2 (3.78–3.64 Å).[20] This is due to the lanthanide contraction phenomenon, where the decrease in ionic radius of the lanthanide series elements from left to right is greater than the expected data. This phenomenon is attributed to the poor shielding effect of the $4f$ electrons on the nuclear charge, coupled with the anticipated periodic trend of increasing electronegativity and nuclear charge from left to right.[35,36]

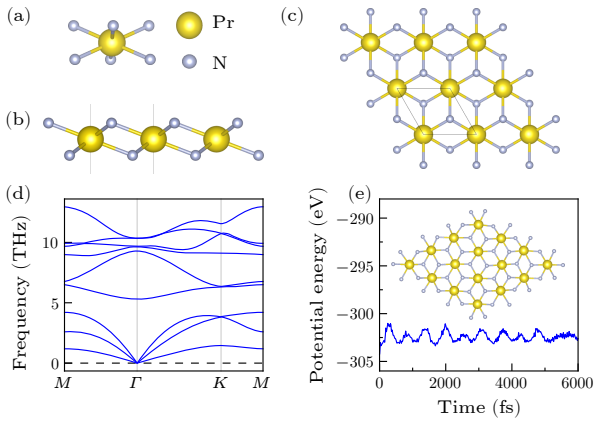

Fig. 1. Geometry and stability of 1T-PrN_2. The octahedral structure unit (a), side view (b) and top view (c) of PrN_2 monolayer. Phonon spectrum of PrN_2 monolayer (d). Variations of the total free energy of PrN_2 monolayer (e) in the (4×4) supercell with respect to simulation time of AIMD at 300 K. The inset shows the final state of the structure after the AIMD simulations.

In order to confirm the stability of PrN_2, we first calculate the cohesive energy expressed as $E_{coh} = (E_{PrN_2} - E_{Pr} - 2E_N)/3$ where E_{PrN_2}, E_{Pr}, and E_N are the total energies of per unit cell of PrN_2 monolayer, Pr atom, and N atom, respectively. The negative cohesion energy of −2.35 eV indicates that the PrN_2 monolayer is energetically stable. Moreover, we also investigate the phonon dispersion of the PrN_2 monolayer. As shown in fig. 1(c), the negative frequency is absent in the whole Brillouin zone, indicating its dynamical stability. We also performed the MD simulation at 300 K. As shown in Fig. 1(d), the total free energy of PrN_2 remains almost invariant during the simulation and the structure remains intact at 300 K after 6 ps. This suggests that the PrN_2 monolayer is thermally stable at room temperature. Clearly, the dynamical, energetic and thermal stabilities suggest that the 1T PrN_2 monolayer can be realized experimentally even at room temperature.

Magnetic Property. We now evaluate the magnetic properties of the PrN_2 monolayer. To reveal the magnetic ground state of monolayer PrN_2, four possible different magnetic configurations (Fig. 2), including ferromagnetic (FM), Néel antiferromagnetic (NAFM), stripy antiferromagnetic (SAFM), and zigzag antiferromagnetic (ZAFM), are considered in the calculations. The total energies of the NAFM, SAFM, and ZAFM states are 528.80, 325.82, and 385.49 meV per unit cell relative to that of the FM state, respectively, indicating that the magnetic ground state of the PrN_2 monolayer is ferromagnetism. The FM state exhibits $3\,\mu_B$ magnetic moment per unit cell, mostly contributed by N atoms. As the Pauling electronegativity of the N atom (3.04) is much larger than that of the Pr atom (1.13), the Pr atom donates three outermost electrons ($5d^16s^2$) to the two N atoms. According to Hund's rule and the Pauli exclusion principle, total nine electrons in the two N atoms should exhibit an electronic configuration of (↑↓ ↑↓ ↑↓ ↑ ↑ ↑), leaving three unpaired electrons with a magnetic moment of $3\,\mu_B$.

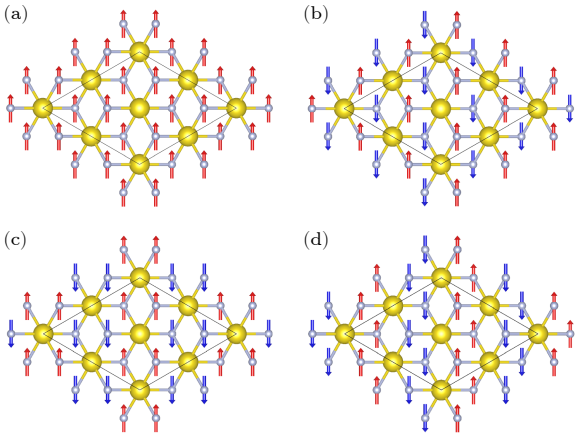

Fig. 2. Possible magnetic configuration of the PrN_2 monolayer. FM, AFM-Néel, AFM-zigzag, and AFM-stripy are shown in (a)–(d), respectively. The red and blue arrows represent the spin direction of N atoms. The crystal cells used in the calculations are also shown.

Magnetocrystalline anisotropy energy (MAE) is one of the most fundamental properties of magnetic materials. We have calculated the total energies of the PrN_2 monolayer with the magnetic moment in different directions with an interval of 5°. The direction-dependent energy landscapes are shown in Fig. 3. We find that the total energy of the PrN_2 monolayer with magnetization direction

lying in the xy plane is 132 meV lower than the case of the z-direction. This indicates that the PrN_2 monolayer belongs to the category of XY magnets.

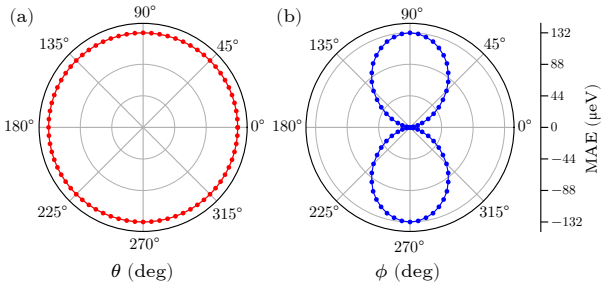

Fig. 3. Magnetization-direction-dependent magnetocrystalline anisotropy energy (a) MAE as a function of the azimuthal angle θ between the magnetization direction and the positive direction of the x-axis in xy plane. (b) MAE as a function of the azimuthal angle ϕ between the magnetization direction and the positive direction of the z-axis in xz plane.

According to the Mermin–Wagner theorem, long-range magnetic order can not be generated in two-dimensional isotropic systems. However, the finite-size effects can stabilize the magnetic order, which was recently verified in the easy-plane magnets 1T-VSe_2 [37] and $CrCl_3$ [38] to the monolayer limit. In 2D XY magnets, the Berezinskii–Kosterlitz–Thouless (BKT) phase transition occurs near the critical temperature $T_{\rm BKT}$. Below the critical temperature, the system is in the ordered phase, while it enters the disordered phase above the critical temperature. To estimate the $T_{\rm BKT}$ of the PrN_2 monolayer, the XY model Hamiltonian is written as

$$H = -J_1 \sum_{\langle i,j \rangle} \boldsymbol{S}_i \cdot \boldsymbol{S}_j - J_2 \sum_{\langle i,j \rangle} \boldsymbol{S}_i \cdot \boldsymbol{S}_j - J_3 \sum_{\langle i,j \rangle} \boldsymbol{S}_i \cdot \boldsymbol{S}_j, \quad (1)$$

where $\boldsymbol{S}_i$ and $\boldsymbol{S}_j$ are the spin vectors in the xy plane at sites i and j; J_1, J_2, and J_3 are parameters of the magnetic exchange interaction between nearest-neighbor (NN), next-nearest-neighbor (NNN), next-next-nearest-neighbor (3NN), respectively. The magnetic energies of FM, NAFM, SAFM, and ZAFM can be explicitly expressed as

$$E_{\rm FM} = E_0 + (-3J_1 - 6J_2 - 3J_3)|\boldsymbol{S}|^2, \quad (2)$$

$$E_{\rm NAFM} = E_0 + (3J_1 - 6J_2 + 3J_3)|\boldsymbol{S}|^2, \quad (3)$$

$$E_{\rm SAFM} = E_0 + (J_1 + 2J_2 - 3J_3)|\boldsymbol{S}|^2, \quad (4)$$

$$E_{\rm ZAFM} = E_0 + (-J_1 + 2J_2 + 3J_3)|\boldsymbol{S}|^2. \quad (5)$$

With the normalized magnetization of $|\boldsymbol{S}| = 1$, the values of J_1, J_2, and J_3 are 58.64, 11.41, and 29.49 meV, respectively. They are all positive values, leading to an FM ground state for the PrN_2 monolayer. The BKT transition temperature can be estimated to be $0.89J_1/k_{\rm B}$,[16,27] where $k_{\rm B}$ is the Boltzmann constant. The estimated $T_{\rm BKT}$ of PrN_2 is about 605 K. Additionally, utilizing the Hamiltonian given by Eq. (1) we conducted magnetic Monte Carlo simulations on a $50 \times 50 \times 1$ supercell. The temperature-dependent magnetization and specific heat are shown in Fig. 4. Several canonical MC simulations [39,40] show that the maximum in the temperature dependence of the specific heat occurs at a temperature of about 15% higher than the Kosterlitz–Thouless transition temperature. The specific heat peak at 611 K, as shown in Fig. 4, also demonstrates the high BKT temperature of PrN_2.

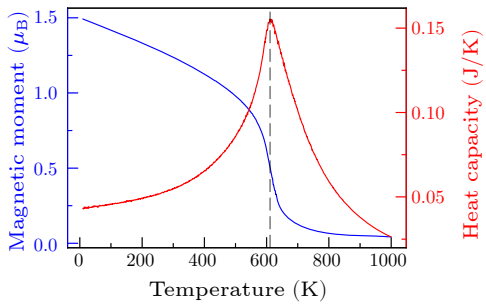

Fig. 4. Magnetic moment and heat capacity with temperature obtaining in Monte Carlo simulation, in which $M = \sqrt{(m_x^2 + m_y^2)}$ and $C_v = (\langle E^2 \rangle - \langle E \rangle^2)/T^2$.

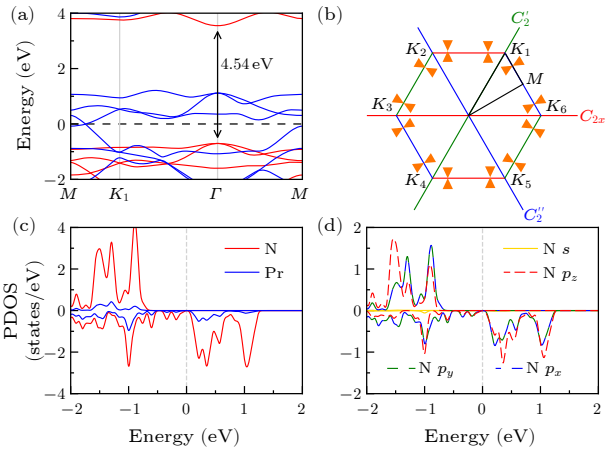

Fig. 5. Electronic band structures of the PrN_2 monolayer without spin-orbit coupling (SOC), and partial density of states (PDOS) of the PrN_2 monolayer. (a) Spin-resolved band structure of the PrN_2 monolayer. The Fermi level is set to 0 eV. (b) Two-dimensional Brillouin zone of the PrN_2 monolayer with three twofold rotational axes, and 12 Dirac cones represented by orange funnel shapes. (c) PDOSs of the N and Y atoms for the PrN_2 monolayer. (d) PDOSs of the s and p orbitals of N atoms for the PrN_2 monolayer.

Now, we turn our attention to the electronic structure of the PrN_2 monolayer. The electronic energy band structure without SOC is shown in Fig. 5(a). The spin-up channel is insulating with a large direct gap (4.54 eV) at the Γ point, while the spin-down channel has a linear Dirac point on the M–K path at the Fermi energy level. Due to the symmetry, there are total 12 Dirac points in the first Brillouin zone, which are protected by the twofold rotational symmetries. As shown in Fig. 5(b), the Dirac cones on K_1–K_2 and K_4–K_5, on K_2–K_3 and K_5–K_6, on K_3–K_4 and K_6–K_1 are protected by axes C_{2x}, C_2', C_2'', respectively. In order to further understand the forma-

tion of Dirac points, we calculated the projected density of states (PDOS) of the monolayer PrN_2. As shown in Figs. 5(c) and 5(d), we can see that the state near the Fermi level mainly gets contributions from the p orbitals of N atoms, which indicates that the PrN_2 monolayer is a p state Dirac half metal (DHM). Moreover, we also predicted a high Fermi velocity [17] of 4.42×10^5 m/s. This value is comparable to that of graphene (8.2×10^5 m/s) [41] and silicene (5.3×10^5 m/s). [42]

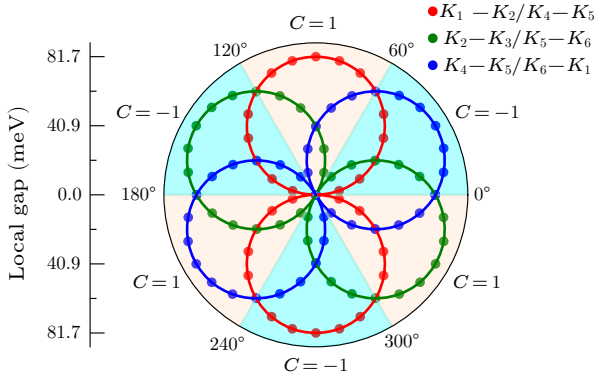

Fig. 6. Band gaps as a function of the angle θ. Red points and lines are gaps on K_1–K_2/K_4–K_5, green points and lines are gaps on K_2–K_3/K_5–K_6, blue points and lines are gaps on K_3–K_4/K_6–K_1, points are the values calculated by DFT and solid lines are fitted by the function gap $= 81.74\,\text{meV} \times \sin\phi$, where ϕ represents the angle between the direction of the magnetic moment and the twofold rotational axes. Different color areas correspond to the different Chern numbers ($C = \pm 1$).

Next we discuss the band structure with SOC effect. Since it has easy plane with isotropic energy in the xy plane, we need to study its energy band structure for different magnetic moment directions. The variation of band gap with angle θ is shown in Fig. 6, where θ represents the angle between the direction of the magnetic moment and the positive direction of the x-axis in xy plane. We first focus on the red points calculated from DFT, which represent the band gap between K_1–K_2/K_4–K_5. The local band gaps at $\theta = 0°$ and $\theta = 180°$ close, because of the direction of magnetic moment parallel to C_{2x} axis preserving the C_{2x} twofold rotational, protecting the degeneration on K_1–K_2 and K_4–K_5. As the angle ϕ between the magnetic moment and the C_{2x} axis increases, the value of the band gap increases. It reaches the maximum (81.74 meV), when the magnetic moment is perpendicular to the C_{2x} axis. It is easy to find that the values of local band gaps and angle ϕ satisfy the sinusoidal relationship. The local band gaps between K_2–K_3/K_5–K_6 and K_3–K_4/K_6–K_1 have similarly sinusoidal relationship with the angle between axes C_2' and C_2'', as shown by the green lines and blue lines in Fig. 6. We can see that global band gap is largest to 40.87 meV when the magnetic moment direction is perpendicular to one of the twofold rotational axes. When the magnetic moment direction is parallel to one of the twofold rotational axes, the global band gap closes. Since it is well known that the PBE functional in generalized gradient approximation (GGA) suffers from the band-gap problem, we additionally employed the SCAN functional for our calculations. The band gaps calculated using the SCAN functional are approximately 1.3 times larger than those derived from GGA functionals. Moreover, as shown in Fig. S4(a) in the Supplementary Material, the bandgap obtained using the SCAN functional under in-plane magnetization also demonstrates a sinusoidal relationship with the angle between the magnetization direction and the twofold rotation axes.

The closing and opening of the band gap are often accompanied by the topological phase transition. Thus, in order to study the topological property, the Chern numbers are computed according to

$$C = \frac{1}{2\pi} \int_{\text{BZ}} d^2k \Omega(k), \tag{6}$$

where Ω is the Berry curvature in the reciprocal space. The nonzero Chern numbers (± 1) of the PrN_2 monolayer with in-plane magnetization suggest that the PrN_2 monolayer is in the QAH state, as shown in Fig. 6. The Chern numbers alternate the sign periodically every 60° as the magnetic moment direction changes.

We further construct a Wannier-based tight-binding model by p orbitals of N atoms to reveal the topological property of PrN_2 with different magnetic directions. Figures 7(a)–7(d) show the case of $\theta = 0°$. The global band gap is closed on path K_1–K_2 (K_4–K_5) as shown in Fig. 7(b), since the magnetization direction preserves C_{2x} symmetry. The local band gaps on path K_2–K_3 (K_5–K_6) and K_3–K_4 (K_6–K_1) are both 70.6 meV since the direction of magnetization is at a 30° with respect to both C_2' and C_2''. Because the crossing points at K_1–K_2/K_3–K_4 are double degeneracy and 100% spin polarization, the cross point can be recognized as Weyl-like points, which is also known as Weyl half semimetals (WHSMs). [20,43,44] We can clearly see a Fermi arc connecting the pair of gapless points in Fig. 7(c). Then, we focus on the case of $\theta = 30°$ and $\theta = 330°$. As shown in Figs. 7(c)–7(h), they all have global band gaps as large as 40.87 meV ($40.87 \approx 81.74 \times \cos(30°)$) since all three twofold rotational symmetries are broken. However, their edge states connecting the conduction and valence bands have opposite directions. In order to understand the mechanism of the topological phase transition, the Berry curvature is also investigated. As shown in Figs. 7(d), 7(h), and 7(l), the Berry curvature can be divided into three parts of K_1–K_2/K_4–K_5, K_2–K_3/K_5–K_6, and K_3–K_4/K_6–K_1. The red color in each part indicates that the contribution to Chern number is +1 and the blue color represents −1. The Chern numbers with $\theta = 30°$ and $\theta = 330°$ are −1 and +1 by adding them up. It is easy to see that the contributions of the three Berry curvatures to the Chern number are different only in the K_1–K_2/K_4–K_5 part, corresponding to the C_{2x} axis. When the direction of magnetic moment is parallel to the C_{2x} axis, it is a critical state, which corresponds to a zero contribution to the Chern number. When the magnetic moment directions are on either side of the C_{2x} axis, their contributions to the Chern number in K_1–K_2/K_4–K_5 are opposite (± 1), that is, the contributions to the Chern number in K_1–K_2/K_4–

K_5 is -1 when $0 <^\circ \theta < 180^\circ$ and 1 when $180^\circ < \theta < 360^\circ$. For the same reason, the contributions to the Chern number in K_2–K_3/K_5–K_6 is -1 when $-120^\circ < \theta < 60^\circ$ and 1 when $60^\circ < \theta < 240^\circ$, separated by the C_2' axis. The contributions to the Chern number in K_3–K_4/K_6–K_1 is -1 when $120^\circ < \theta < 300^\circ$ and 1 when $-60^\circ < \theta < 120^\circ$, separated by the C_2'' axis. Summing up these contributions produces a phase diagram of the Chern number, exhibiting a sign change every 60°, consistent with Fig. 6.

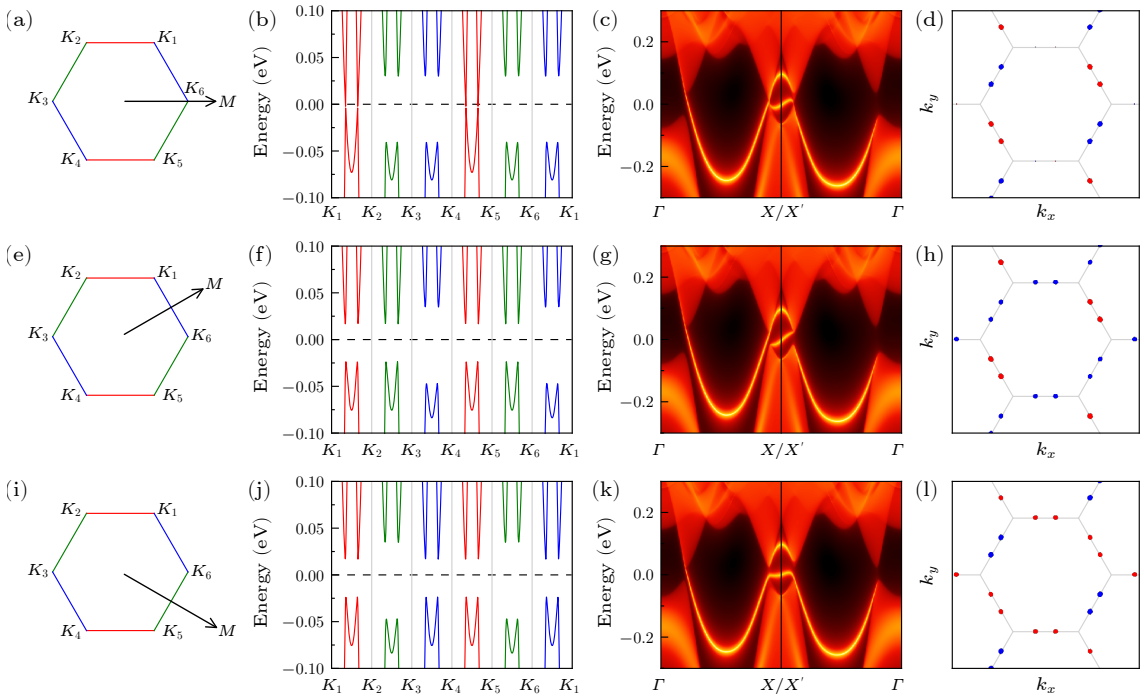

Fig. 7. Band structures and topological properties for monolayer PrN_2 under SOC with xy plane magnetization. The magnetization direction, band structures, edge states, and Berry curvatures with $\theta = 0^\circ$, 30°, 90° are shown in (a)–(d), (e)–(h), (i)–(l), respectively.

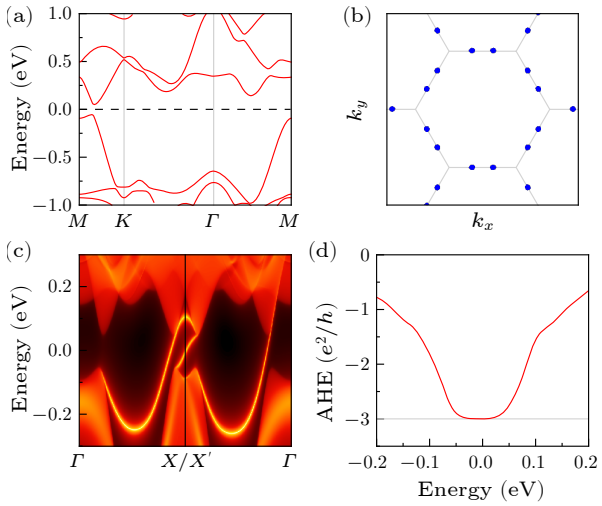

Fig. 8. Band structures and topological properties for monolayer PrN_2 under SOC with out-of-plane magnetization. The band structure (a) of monolayer PrN_2. Berry curvature (b) of monolayer PrN_2. Edge state (c) of monolayer PrN_2. AHC σ_{xy} of monolayer PrN_2.

As its small MAE, we can adjust the magnetization direction out of xy plane by applying a small magnetic field. As shown in Fig. 8 for the case that the direction of the magnetic moment is pointing toward the z-axis. The PrN_2 monolayer opens up a band gap as large as 101.12 meV between the M–K paths. Additionally, the value of band gap calculated by the SCAN functional is 132 meV as shown in Fig. S4(b) in the Supplementary Material, which is approximately 30% larger than that computed using the PBE functional. The contribution of the Berry curvature to the Chern number for all three parts is -1, so the PrN_2 monolayer enters a QAH state with high Chern number C of -3. We can clearly see that there are three edge states connecting the conduction and valence bands as shown in Fig. 8(c). Moreover, the AHC σ_{xy} of PrN_2 monolayer is shown in Fig. 8(d), which is exactly quantized to e^2/h. These indicate that monolayer PrN_2 can realize QAH effect with large band gap and high Chern number by manipulating magnetization direction.

In conclusion, we have systematically investigated the structural stability, magnetic properties, electronic structure, and topological properties of monolayer PrN_2 by DFT calculations. It belongs to the category of XY magnets with high BKT temperature of 605 K. It is a p state DHM with a high Fermi velocity of 4.42×10^5 m/s without SOC. When SOC is considered, rich topological states determined by the magnetization direction can be found. When the magnetization direction lying in the xy plane, the WHSMs state and QAH state with low Chern number (± 1) are formed. The size of the band gap can be

precisely described by the sine function of the angle between the magnetization direction and the twofold rotational axes. When the direction of the magnetic moment turns to be out-of-plane, the large band gap (101.12 meV) and QAH state with higher Chern number (±3) can be obtained. Our study provides a new material with high magnetic transition temperature for tunable Chern number QAH state, which offers a promising platform for high-performance spintronics devices.

Acknowledgments. This work was supported by National Natural Science Foundation of China (Grant No. 11874092), the Fok YingTong Education Foundation, China (Grant No. 161005), and the Science Fund for Distinguished Young Scholars of Hunan Province (Grant No. 2021JJ10039).

References

[1] Haldane F D M 1988 *Phys. Rev. Lett.* **61** 2015
[2] Chang C Z, Liu C X, and MacDonald A H 2023 *Rev. Mod. Phys.* **95** 011002
[3] Qi X L and Zhang S C 2011 *Rev. Mod. Phys.* **83** 1057
[4] Hasan M Z and Kane C L 2010 *Rev. Mod. Phys.* **82** 3045
[5] Chang C Z, Zhang J, Feng X, Shen J, Zhang Z, Guo M, Li K, Ou Y, Wei P, Wang L L, Ji Z Q, Feng Y, Ji S, Chen X, Jia J, Dai X, Fang Z, Zhang S C, He K, Wang Y, Lu L, Ma X C, and Xue Q K 2013 *Science* **340** 167
[6] Lee I, Kim C K, Lee J, Billinge S J L, Zhong R, Schneeloch J A, Liu T, Valla T, Tranquada J M, Gu G, and Davis J C S 2015 *Proc. Natl. Acad. Sci. USA* **112** 1316
[7] Lachman E O, Young A F, Richardella A, Cuppens J, Naren H R, Anahory Y, Meltzer A Y, Kandala A, Kempinger S, Myasoedov Y, Huber M E, Samarth N, and Zeldov E 2015 *Sci. Adv.* **1** e1500740
[8] Qi S, Liu Z, Chang M, Gao R, Han Y, and Qiao Z 2020 *Phys. Rev. B* **101** 241407
[9] Deng Y, Yu Y, Shi M Z, Guo Z, Xu Z, Wang J, Chen X H, and Zhang Y 2020 *Science* **367** 895
[10] Gong Y, Guo J, Li J, Zhu K, Liao M, Liu X, Zhang Q, Gu L, Tang L, Feng X, Zhang D, Li W, Song C, Wang L, Yu P, Chen X, Wang Y, Yao H, Duan W, Xu Y, Zhang S C, Ma X, Xue Q K, and He K 2019 *Chin. Phys. Lett.* **36** 076801
[11] Jiang H, Qiao Z, Liu H, and Niu Q 2012 *Phys. Rev. B* **85** 045445
[12] Wang J, Lian B, Zhang H, Xu Y, and Zhang S C 2013 *Phys. Rev. Lett.* **111** 136801
[13] Duong L Q, Lin H, Tsai W F, and Feng Y P 2015 *Phys. Rev. B* **92** 115205
[14] Zeng J, Ren Y, Zhang K, and Qiao Z 2017 *Phys. Rev. B* **95** 045424
[15] Zhu W, Song C, Bai H, Liao L, and Pan F 2022 *Phys. Rev. B* **105** 155122
[16] Li Z, Han Y, and Qiao Z 2022 *Phys. Rev. Lett.* **129** 036801
[17] Liu Z, Liu J, and Zhao J 2017 *Nano Res.* **10** 1972
[18] Kong X, Li L, Leenaerts O, Wang W, Liu X J, and Peeters F M 2018 *Nanoscale* **10** 8153
[19] Jin L, Wang L, Zhang X, Liu Y, Dai X, Gao H, and Liu G 2021 *Nanoscale* **13** 5901
[20] Yu Y, Chen X, Liu X, Li J, Sanyal B, Kong X, Peeters F M, and Li L 2022 *Phys. Rev. B* **105** 024407
[21] Li S, Li X, Ji W, Li P, Yan S, and Zhang C 2023 *Phys. Chem. Chem. Phys.* **25** 18275
[22] Kresse G and Furthmüller J 1996 *Comput. Mater. Sci.* **6** 15
[23] Kresse G and Furthmüller J 1996 *Phys. Rev. B* **54** 11169
[24] Blöchl P E 1994 *Phys. Rev. B* **50** 17953
[25] Kresse G and Joubert D 1999 *Phys. Rev. B* **59** 1758
[26] Perdew J P, Burke K, and Ernzerhof M 1996 *Phys. Rev. Lett.* **77** 3865
[27] Monkhorst H J and Pack J D 1976 *Phys. Rev. B* **13** 5188
[28] Togo A 2023 *J. Phys. Soc. Jpn.* **92** 012001
[29] Pizzi G, Vitale V, Arita R, Blügel S, Freimuth F, Géranton G, Gibertini M, Gresch D, Johnson C, Koretsune T, Ibañez-Azpiroz J, Lee H, Lihm J M, Marchand D, Marrazzo A, Mokrousov Y, Mustafa J I, Nohara Y, Nomura Y, Paulatto L, Poncé S, Ponweiser T, Qiao J, Thöle F, Tsirkin S S, Wierzbowska M, Marzari N, Vanderbilt D, Souza I, Mostofi A A, and Yates J R 2020 *J. Phys.: Condens. Matter* **32** 165902
[30] Kim H J 2018 VASPBERRY: Berry curvature calculation code for VASP output, Zenodo
[31] Kim S W, Kim H J, Cheon S, and Kim T H 2022 *Phys. Rev. Lett.* **128** 046401
[32] Wu Q, Zhang S, Song H F, Troyer M, and Soluyanov A A 2018 *Comput. Phys. Commun.* **224** 405
[33] Li L, Kong X, Chen X, Li J, Sanyal B, and Peeters F M 2020 *Appl. Phys. Lett.* **117** 143101
[34] Lin Z Z and Chen X 2020 *Appl. Surf. Sci.* **529** 147129
[35] Pyykkö P 1988 *Chem. Rev.* **88** 563
[36] Seth M, Dolg M, Fulde P, and Schwerdtfeger P 1995 *J. Am. Chem. Soc.* **117** 6597
[37] Zhuang H L and Hennig R G 2016 *Phys. Rev. B* **93** 054429
[38] Bedoya-Pinto A, Ji J R, Pandeya A K, Gargiani P, Valvidares M, Sessi P, Taylor J M, Radu F, Chang K, and Parkin S S P 2021 *Science* **374** 616
[39] Tobochnik J and Chester G V 1979 *Phys. Rev. B* **20** 3761
[40] Ota S, Ota S B, and Fahnle M 1992 *J. Phys.: Condens. Matter* **4** 5411
[41] Jiao Y, Ma F, Bell J, Bilic A, and Du A 2016 *Angew. Chem.* **128** 10448
[42] Wang Y and Ding Y 2013 *Solid State Commun.* **155** 6
[43] You J Y, Chen C, Zhang Z, Sheng X L, Yang S A, and Su G 2019 *Phys. Rev. B* **100** 064408
[44] Huan H, Xue Y, Zhao B, Bao H, Liu L, and Yang Z 2022 *Phys. Rev. B* **106** 125404